SARAS: A Synthetic Aperture Radar (SAR) Raw Signal Simulator

Giorgio Franceschetti, *Fellow, IEEE,* Maurizio Migliaccio, *Member, IEEE,* Daniele Riccio, *Member, IEEE,* and Gilda Schirinzi, *Member, IEEE*

Abstract—**A Synthetic Aperture Radar (SAR) simulator of an extended three-dimensional scene is presented. It is based on a facet model for the scene, asymptotic evaluation of SAR unit response, and two-dimensional fast Fourier transform (FFT) code for data processing. Prescribed statistics of the model account for a realistic speckle of the image. The simulator is implemented in a code (SARAS) whose performance is described and illustrated by a number of examples.**

I. Introduction

WITHIN the framework of Synthetic Aperture Radar (SAR) studies it is convenient to simulate the signal received on board before any processing (with the exception of the heterodyne down-converter). From now on this signal is referred to as the raw signal. Simulation of canonical scenarios may simplify experimentation of processing algorithms, as well as development of pattern recognition and feature extraction techniques. Simulation may play a significant role in studies concerning noise and clutter rejection and may contribute toward optimizing SAR system parameters.

A simulation code must meet a number of stringent constraints. The scenario to be simulated should be rather general and possibly time varying, either deterministically or stochastically. It should rely upon a sound-scattering model which must comply with proper statistical rules. An important feature for a SAR simulator of an extended scene is the altitude profile, since the influence of the relief plays a great role in the formation of the final image. Last, but not least, the numerical code should be efficient, fast, and (computer) memory saving. These features are usually in competition, and the ultimate solution is generally an engineering compromise.

Many simulation studies are available in the literature [1]–[4], leading to simulation codes which comply with some (but usually not all) prerequisites. In all codes the surface of the scene is discretized in a (usually) rectangular grid; and superposition of elementary returns from the grid points is implemented. Different procedures can be used, depending on the evaluation of the single return, its statistical relation with other returns, and the accuracy of the superposition in view of the SAR system parameters. A discussion about these points is worthwhile.

A first point to be addressed is the single return evaluation. One possibility is to use simple point scatterers, whose intensity is given by the square-root of the local radar cross section. For a realistic simulation, access to a data bank for the latter is required [1], [3], [5], [6]. As an alternative approach, the surface can be locally approximated by plane facets, centered on the grid points; the return can be computed by simple application of electromagnetic theory, provided that the electromagnetic parameters of the material are prescribed. This second procedure seems to be flexible, requires a limited amount of information, and relies on a sound physical model: It is the procedure adopted by the simulator we propose.

A second important point to be considered is the number of scatterers, or facets, per resolution cell. Clearly, a large facet number improves the description of the altitude profile, but requires efficient tools to handle memory requirements and computational time. Both problems are addressed in Synthetic Aperture Radar Advanced Simulators (SARAS), which rely upon an innovative two-stage fast Fourier transform (FFT) algorithm, which is further amenable to parallel processing.

A central problem in a SAR simulator is the implementation of the correct statistical features of the signal. Two extreme procedures can be foreseen: We can either operate on the physical model of the scene or directly on the image. A brief discussion seems to be appropriate.

If statistical features are implemented on the physical model, first the surface roughness must be considered. For a Gaussian scene [7] the correlation length is negligible compared to both the facet dimension and the system resolution. Accordingly, the interpixel statistics are governed by the system bandwidth: The simulator correctly generates the appropriate statistics, which is controlled by the input system data. The alternative extreme case is that of a highly correlated scene (negligible roughness): the interpixel statistics depend on both the scene correlation and system bandwidth, and can be again correctly handled by the simulator.

On the contrary, the speckle can be directly applied (by multiplication) to the image. This is simple in principle, but properly requires tracing down the effect of statistical morphology of the scene on the image; simple application of speckle per pixel is not appropriate, because it does not take into account filtering properties of the SAR system [8]. In the simulator we present the statistical description is introduced at the physical model and not on the final image.

Manuscript received July 30, 1990; revised July 19, 1991. This work was sponsored in part by a grant provided by Alenia SpA.

The authors are with the Consiglio Nazionale delle Ricerche, Istituto di Ricerca per l'Elettromagnetismo e i Componenti Elettronici, Via Diocleziono 328, 80124 Napoli, Italy.

G. Franceschetti is also with the Department of Electronic Engineering, University of Naples, Italy.

IEEE Log Number 9103856.

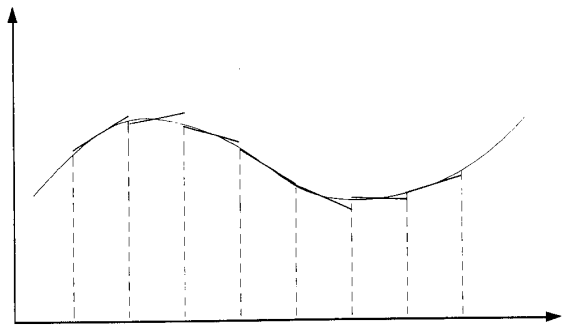

Fig. 1. Facet model of the scene.

As a conclusion, we introduce a SAR raw signal simulator, SARAS, which computes the reflecitivity map relying on an electromagnetic polarimetric model of an extended three-dimensional scene. It accurately evaluates the raw signal by means of the appropriate system function, analytically computed in the (two-dimensional) Fourier transformed domain, including the aberrations of the SAR system.

We present now the general structure of our simulator, as developed in subsequent sections. The height profile of the scene is described by an appropriate function, which may be prescribed either analytically or numerically. This profile is then approximated by square plane facets (see Fig. 1), large in terms of the incident wavelength but small when compared to the resolution length. Each facet is characterized by the coordinates of three vertices (or, alternatively, by the coordinates of its center and the associate normal) and by the electromagnetic parameters (permittivity ϵ and conductivity σ) of the underlying material.

The SAR raw signal is the appropriate superposition of returns from each facet. Accordingly, a first problem is the computation of individual facet backscattering, taking into account local angle of incidence, polarization of the incident wave, the facet's roughness, and any shadowing effect, if present. This is considered and discussed in Section II.

Once the elementary fields backscattered by each facet have been computed, their superposition is in order; this is discussed in Section III. Irregularities of the (macroscopic) terrain profile imply statistical displacements of the facet's vertices, which can be modeled by associating with each facet a random displacement of three of its four vertices. As an alternative possibility, we note that this vertex displacement is equivalent to moving the facet center and to changing the orientation of its normal. Accordingly, we can add a random displacement with an appropriate probability distribution function (pdf) to each facet position, as well as a random normal orientation.

The efficient summation of all returns is considered in Section IV. This is accomplished via two-dimensional FFT code [9] and an asymptotic evaluation of the system transfer function [9]. Range migration and curvature effects are included in the transfer function. Change of focus depth with the distance is also incorporated by a grid deformation in the transformed space.

The complete structure of the simulator is discussed in Section V and depicted in the flow-chart of Fig. 8; it is noted that input data comprise geometrical, cinematical, electromagnetic, and statistical parameters.

A number of examples of simulated data are collected under Section VI, in order to assess the performance of the code. Conclusions and recommendations are referred to under Section VII.

II. Facet Backscattering

The basic problem to be solved in a SAR simulator is the electromagnetic characterization of the scene under survey, i.e., the relationship between incident and backscattered field; the ratio between the two fields over the scene is the backscattering coefficient $\gamma(x, r)$, x and r being azimuthal and range coordinates. In the most general case the incident field interacts with the scene via surface and volume backscattering. In the following sections, we are only concerned with the surface contribution, while multiple scattering is totally neglected. We restrict ourselves to a terrain scene, excluding the ocean, for which the scattering mechanism (Bragg phenomena) is different from the one we adopt here. This allows us to also consider the scene invariant within the integration time.

Among all possible terrain models, the facet model is a very useful one (see Fig. 1), which amounts to a piecewise planar approximation of the scene. We assume the dimensions of the facets to be small in terms of resolution, but large in terms of incident wavelength. Note further that each facet must be small enough to correctly approximate the surface height profile.

Let the incident field be

$$\boldsymbol{E}_i = \hat{\boldsymbol{e}} E_o \exp(-j\boldsymbol{k} \cdot \boldsymbol{R}) \tag{1}$$

wherein $\boldsymbol{k} = k\hat{\boldsymbol{k}}$ is the incident wave propagation vector, $\hat{\boldsymbol{e}}$ is a unit polarization vector, E_o is the incident field amplitude, and $\boldsymbol{R}$ (see Fig. 2) is the vector distance from the phase center of the transmitting antenna to the facet. We are assuming $\hat{\boldsymbol{e}}$ to be real. In the following, we consider either H-polarized ($\hat{\boldsymbol{e}}$ is along the x-axis) or V-polarized ($\hat{\boldsymbol{k}} \times \hat{\boldsymbol{e}}$ is along the x-axis) waves. Combination of these two polarizations, with different (complex) amplitudes, may synthesize any desidered polarization.

The Kirchhoff solution to the backscattered far-field in the physical optics approximation [10] is

$$\boldsymbol{E}_s(\boldsymbol{R}) = \frac{jk \exp(-jkR)}{4\pi R} E_o \left(\underline{\underline{I}} - \hat{\boldsymbol{k}}\hat{\boldsymbol{k}}\right) \cdot \int_A \boldsymbol{F}(a, b, c) \exp[2j\boldsymbol{k} \cdot \boldsymbol{\rho}]\, dA \tag{2}$$

wherein most of symbols are self-explanatory or defined under Fig. 3, $\underline{\underline{I}}$ is the diagonal unit matrix and (a, b, c) are the components of the vector n normal to A and defined in the Appendix, see (A.1). The function $\mathbf{F}(a, b, c)$ depends on the Fresnel reflection coefficients of the facet, different for the two polarizations, as well as on the wave incidence angle; its detailed expression is given in the Appendix.

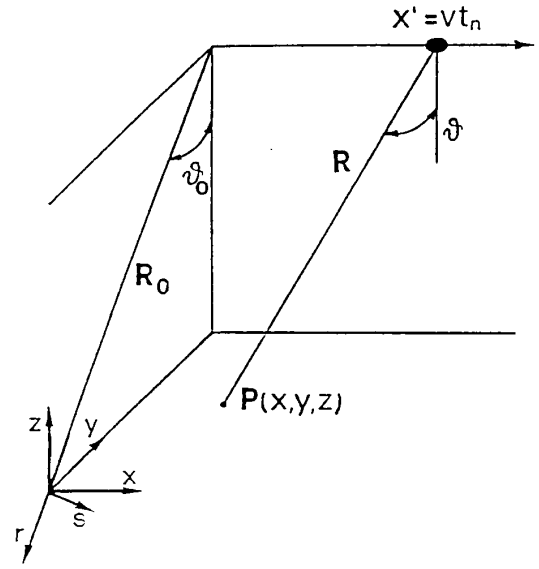

Fig. 2. Geometry of the problem and coordinates reference systems.

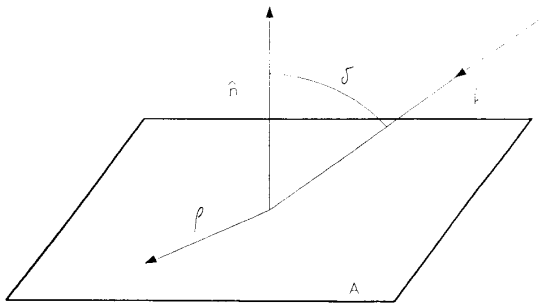

Fig. 3. Relevant to facet backscattering.

For any planar facet $\boldsymbol{F}(a,b,c)$ is constant in the domain of integration, so that the backscattered field is expressed by

$$\boldsymbol{E}_s(\boldsymbol{R}) = \frac{jk\exp(-jkR)}{4\pi R} E_o\left(\underline{\underline{I}} - \hat{\boldsymbol{k}}\hat{\boldsymbol{k}}\right) \cdot \boldsymbol{F}(a,b,c) \int_A \exp(2j\boldsymbol{k}\cdot\boldsymbol{\rho})\, dA. \tag{3}$$

Note that the integral which appears in (3) is the reirradiation diagram of a perfectly conducting facet of the same dimensions as the considered one. Equation (3) can be conveniently expressed in the (x,r,s) coordinate systems of Fig. 2, thus highlighting horizontal and vertical polarized components of the field.

In the general case, the incident field is a combination of H and V components:

$$\boldsymbol{E}_i \rightarrow \frac{jk\exp(-jkR)}{4\pi R} \begin{Vmatrix} E_{oH} \\ E_{oV} \end{Vmatrix} \tag{4}$$

and the elementary field backscattered by the single facet exhibits these two components, as well:

$$\boldsymbol{E}_s \rightarrow \begin{Vmatrix} E_{SH} \\ E_{SV} \end{Vmatrix}. \tag{5}$$

At the receiver

$$\boldsymbol{E}_s = g(\cdot)\underline{\underline{S}} \cdot \boldsymbol{E}_i \int_A \exp(2j\boldsymbol{k}\cdot\boldsymbol{\rho})\, dA \tag{6}$$

wherein $g(\cdot)$ is a system function which describes the appropriate phase delay (and intensity attenuation) of each facet return (see Section IV), and

$$\underline{\underline{S}} \rightarrow \begin{Vmatrix} S_{HH} & S_{VH} \\ S_{VH} & S_{VV} \end{Vmatrix} \tag{7}$$

is a (backscattering) polarization matrix whose entries are computed and listed in the Appendix.

The (polarimetric) backscattering coefficients of the elementary facet are easily recognized from (5), hence

$$\gamma_H = S_{HH} \int_A \exp(2j\boldsymbol{k}\cdot\boldsymbol{\rho})\, dA \tag{8}$$

$$\gamma_V = S_{VV} \int_A \exp(2j\boldsymbol{k}\cdot\boldsymbol{\rho})\, dA \tag{9}$$

$$\gamma_{VH} = \gamma_{HV} = S_{HV} \int_A \exp(2j\boldsymbol{k}\cdot\boldsymbol{\rho})\, dA. \tag{10}$$

Returns from all the facets are summed up at the receiving antenna and produce the polarimetric response of the scene to the SAR illumination.

Before proceeding further, some comments are in order. For a rectangular facet, the reirradiation diagram is the product of two $\mathrm{sinc}(\cdot)$ functions. This is appropriate to smooth facets. If a small roughness is superimposed over the facet, the scattered field also consists of an incoherent part which tends to broaden the reirradiation diagram: It must be modified accordingly. It is known [11]–[13] that the radiative feature of a rough facet strictly depends on the statistical behavior of its roughness. A meaningful parameter is the ratio σ^2/L^2, where σ^2 is the variance of the random height of the facet and L the associated correlation length. When this ratio is large, the incoherent part of the field becomes predominant; in the limit of a very large ratio, the facet scattering tends to a Lambertian-like behavior. In SARAS the appropriate reirradiation diagram can be selected according to the foreseen roughness.

If the facet's length is small compared to the correlation length L, then the $\mathrm{sinc}(\cdot)$ type irradiation diagram is appropriate. This choice, however, implies use of a large facet density per resolution cell, thus unavoidably hampering numerical computations (see Section IV). Reduction of the facet's density leads to large facet dimensions compared to the correlation length, thus modifying the reirradiation diagram. Possible choices are the following ones [12], [13] (see Fig. 3):

$$\text{isotropic:} \quad \cos\delta; \quad \cos^2\delta; \quad \exp\left[-\left(\frac{\delta}{\delta_o}\right)^2\right] \tag{11}$$

with δ_o given. Note that the above diagrams are essentially heuristic. Alternative, more rigorous, options can be freely used in the numerical program. Note that different reirradiation diagrams may be used, if required, in different areas of the scene (as well as different phase statistics). This would simulate regions exhibiting different microscopic statistical morphology.

The intensity of the backscattered field, according to (11), should be intended as a mean square value. We now estimate the amplitude and phase of one element of the ensemble of the fields scattered from each facet. The situation we are considering is that of a large number of uncorrelated scatterers per facet, so that the facet's return is characterized by a uniform phase and Rayleigh amplitude distribution [14], [15]; the latter is completely determined by knowledge of the mean square value, i.e., by the prescribed reirradiation diagram. All elements are thus available to generate one element of the ensemble of each facet's return.

In some cases the scattering properties of the facet are modeled by means of the Bragg phenomena [13], [16], [17]. Bragg scattering is very important for the ocean and may cause a spatially sharp reirradiation diagram; once again, this pattern could be included in our facet model, although it has not been implemented in our code for the moment.

A reliable and accurate SAR signal simulation of a three-dimensional scene cannot avoid taking into account layover and shadows. Layover occurs when different points map onto the same resolution cell; a region is shadowed when it is not illuminated by the radar beam. Simulation of layover regions is basic problem to be solved; it depends on the $(x, y, z) \rightarrow (x, r, s)$ coordinate transformation, therefore, being strictly connected to the geometric distortion which occurs. Grid map is in the (x, y, z) coordinate system, while reflectivity map must be evaluated in the (x, r, s) coordinate system. In our simulator layover phenomenon is correctly included by a method very similar to the shared-power approach [18].

Appearance of shadowed regions is also typical of nonflat scenes. A closed formula exists [10], based on knowledge on the local angle of incidence, which enables us to detect shadowed regions. Unfortunately, it represents a sufficient but not necessary condition, thus failing in some critical situations. In our simulator we adopt a ray-tracing recursive algorithm to overcome this limitation. We select the knee point where the incident ray is tangent to the profile; the next points may or may not belong to a shadowed zone (see Fig. 4), and this is confirmed by a suitable test. This allows us to sort out the shadowed regions with no lack of generality. Of course, ray optics imply neglecting diffraction effects: the shadow is included in (3) by a shadowing function, which is zero inside the shadowed region and one outside (see Fig. 4).

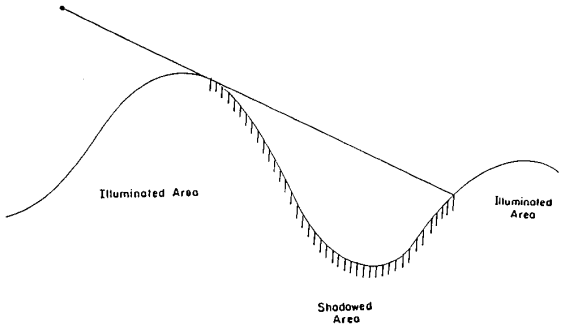

Fig. 4. Geometry relevant to shadowing effect.

III. Statistics of the Facet Returns Summation

In this section we address the problem of the facet returns summation, with the correct large-scale statistical simulation, at variance with the small-scale statistical simulation based on the local roughness of each facet (see Section II).

Let us first consider the height profile simulation. The size of the facet is related to the surface profile variations, and more than one facet may be included in a single cell of the reflectivity map. This is usually the case (also for other reasons discussed later); in any case, we assume that the size of every facet is large compared to the wavelength, so that results of the previous section are valid.

Knowledge of the grid map of the scene's height profile is the starting point used to locate each facet. This grid is given either by means of a numerical file, or by means of a sampled analytical function $z(x, y)$. As a result, the starting information is a discrete set of values $z_{ij} = z(x_i, y_j)$, and several options for the facets' construction are possible. These are summarized below; the final choice is a compromise between accuracy and simplicity of the numerical code.

If continuity of the modeled surface together with all its derivatives is requested, nonplanar facets passing by four adjacent points are required. This results in heavy computational problems on one hand, if the facet equation must be interpolated, and on the other hand, on an extremely complicated functional form for the function $\mathbf{F}(a, b, c)$: Computation of (2) in a reasonably closed form becomes impossible.

If continuity only of the modeled surface is required, then a quadratic surface for each facet is appropriate; again, complexity of (2) still remains.

This discussion underlines that the use of planar facets is highly desirable. If this is accepted, but continuity is required, then we need to consider two planar triangular facets for each four adjacent grid points. This results in some complexity for the reirradiation diagram; as a matter of fact, the integral which appears in (3) must be decomposed into two integrals, each one computed on triangular domains. On the other hand, if some loss in height profile continuity can be tolerated, then we can use square (or rectangular) facets. Let

$$P_{00} \equiv (x_0, y_0, z_{00}), \qquad P_{10} \equiv (x_1, y_0, z_{10})$$
$$P_{01} \equiv (x_0, y_1, z_{01}), \qquad P_{11} \equiv (x_1, y_1, z_{11}) \tag{12}$$

the four adjacent points of the grid. We can determine the facet of fixing, for instance, the coordinates of P_{00}, P_{01}, and P_{10}. Alternatively, we can locate each facet by fixing the coordinates of one of its vertexes, say P_{00}, and computing its normal according to P_{01} and P_{10}. We use this latter description, although any other model adopting planar facet can be efficiently and easily adopted.

It must be noted that until now we have focused our attention on a height function $z = z(x, y)$ deterministically known; but we already noted that even the large-scale profile of natural surfaces needs a statistical description, as does the small-scale one. Samples of ground description file must be thought of as mean values of an altitude random variable; this implies that we should estimate (or prescribe) its pdf and (if needed) its statistics of higher order. It any single facet is uniquely defined by three points of the ground description file, the large scale statistics can be easily managed. Let P_{00}, P_{10}, P_{01} be these three points and z_{ij} their height coordinates; statistics are implemented by superimposing to each z_{ij} a random variable with zero mean and appropriate variance. Some comments are now in order.

A first reasonable assumption is to consider the points of the grid map as independent random variables, with statistics possibly changing from zone to zone. In addition, in many cases it is often reasonable to take a Gaussian pdf:

$$p_z(z) = \frac{1}{\sqrt{2\pi}\sigma} \exp\left(-z^2/2\sigma^2\right) \tag{13}$$

wherein σ is the (prescribed) standard deviation of the height profile. We note, again, that σ may change in different parts of the scene.

The statistical description of the height profile has two main consequences: The center of the facet and its orientation are both statistically displaced. Displacement of the facet center implies that the facet's range is statistically changed; statistical orientation of the facet normal implies that facet returns sum up with a random amplitude, due to rotation of the reirradiation diagram.

If the facet is centered in a point of the grid map (as in SARAS) the statistical displacement of its center is given by (13), hence:

$$p_c(z) = p_z(z). \tag{14}$$

As far as tilt of the normal to the facet is concerned, we already noted that it is determined by the orientation of the facet's sides $P_{00}P_{10}$ and $P_{00}P_{01}$. The two problems are similar, and we consider only one of them. We seek the pdf of the angle ϕ of the side $P_{00}P_{10}$ with the x-axis:

$$\phi = \tan^{-1}\left(\frac{z_{10} - z_{00}}{x_1 - x_0}\right) = \tan^{-1}\zeta. \tag{15}$$

We have [19]:

$$p_\phi(\phi) = \left[1 + \tan^2\phi\right] p_\zeta(\tan\phi). \tag{16}$$

The pdf (16) can be computed by convolving the pdf's of the random variable $z/(x_1 - x_0)$ with itself under the assumed statistical independence of the stochastic displacements of P_{00} and P_{01}. Accordingly, (16) can be recast as follows:

$$\begin{aligned} p_\phi(\phi) &= \left[1 + \tan^2\phi\right][x_1 - x_0]^2 \\ &\quad \cdot \{p_z[z \cdot (x_1 - x_0)] * p_z[z \cdot (x_1 - x_0)]\} \\ &= \frac{\left[1 + \tan^2\phi\right]|x_1 - x_0|}{\sqrt{2\pi}\,\sqrt{2}\sigma} \exp\left(\frac{-(x_1 - x_0)^2 \tan^2\phi}{4\sigma^2}\right) \end{aligned} \tag{17}$$

where the star denotes convolution. The pdf (17) is Gaussian, except for the term $\left(1 + \tan^2\phi\right)$, with a square mean deviation $\sqrt{2}\,\sigma/|x_1 - x_0|$.

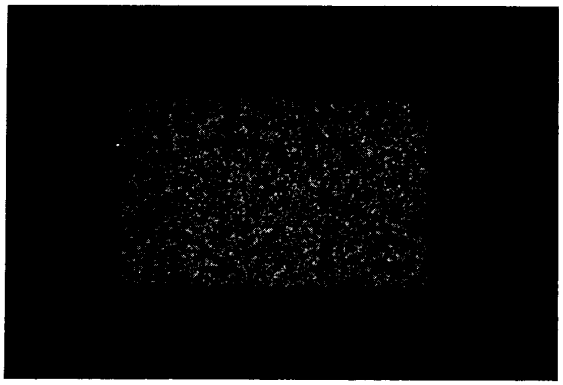

Fig. 5. SAR-simulated image of a flat terrain with homogeneous electromagnetic parameters (HH polarization, $\varepsilon_r = 4$, $\sigma = 10^{-3}$ S/m).

The small and large-scale characterization of the electromagnetic scattering results in the inclusion of the appropriate statistics of the speckle on the raw signal and, after compression, on the image. As a matter of fact, a digitally processed SAR image exhibits this well-known phenomenon [20]–[23], which is typical of (quasi) monochromatic illumination, and is due to random interference among scattered fields by reirradiating elements present within the resolution cell. It should be noted that we have been concerned in this section only about first-order statistics. This is appropriate, provided that the reflectivity pattern power spectrum is wider than the SAR system bandwidth, so that the latter determines the autocorrelation function of the image. This assumption breaks down for highly correlated scenes, e.g., calibration corner reflectors or man-made smooth structures. For this case we use the deterministic reflection coefficient (8–10) and neglect the subsequent statistical grid map deformation.

Speckle, on one hand, is undesired and constitutes noise with respect to the image to be detected [24], [25]; on the other hand, it has some informative content [7]. An appropriate inclusion of speckle is, therefore, very important in a SAR signal simulator, for noise rejection studies, interferometric applications, and feature extraction. Classification and texture analysis simulation is possible only if appropriate speckle is included. In addition, a model change does not require a new retrieval of image or raw signal statistics.

We present here quantitative results of image statistics via simulated raw data (generation of the images is discussed under Section VI). In order to compute data distribution on a single and interpixel basis, we selected a macroscopic homogeneous area. Statistical results over the simulated image of Fig. 5 are displayed under Fig. 6 (grey-level distribution) and Table I (image correlation). As consequence of imaging a Gaussian scene, it must be noted that the grey-level distribution is Rayleigh since one-look processing has been accomplished [13]. Such distribution does depend on the number of the independent looks [8], [13]; on the contrary, the pixel dimension does not affect it [21].

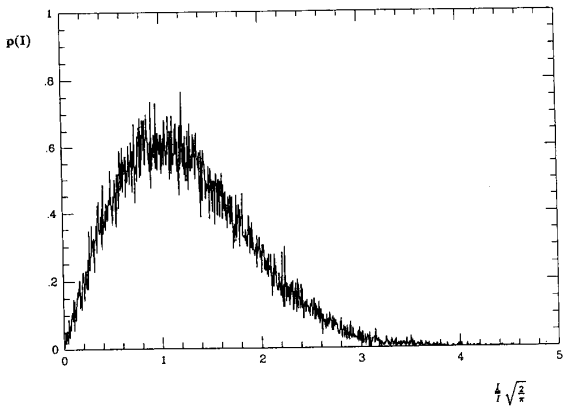

Fig. 6. Grey-level distribution over the simulated image of Fig. 5 (I is the Intensity).

TABLE I
NUMERICAL VALUES OF THE AUTOCORRELATION FUNCTION RELATIVE TO THE SIMULATION RUN OF FIG. 5.

Azimuth / Range		Pixel 0	1	2	3	4
Pixel	0	1.00	0.51	0.15	0.11	0.12
	1	0.70	0.35	0.11	0.06	0.08
	2	0.14	0.05	0.01	0.00	0.02
	3	0.21	0.11	0.04	0.03	0.02
	4	0.10	0.04	0.02	0.01	0.01

This autocorrelation turns out to be coincident to the point spread function of the system (see Fig. 7).

The focusing parameters adopted in the processing are exactly the same as the ones used to generate the raw signal. Accordingly, the image autocorrelation function, numerically sketched under Table I, turn out to be coincident with the point spread function of the system [8], [20] (see Fig. 7).

As a last remark, let us note that the choice of facet number is a compromise among height profile approximation, statistical description, and computational efficiency. We only note that computational problems can be handled by the comb FFT technique (see Section IV); and that the number of 4×4 facets per resolution cell is already sufficient for a satisfactory simulation [26].

IV. SAR RAW SIGNAL COMPUTATION

In this section we briefly summarize the theory of SAR raw signal formation, to explain its efficient evaluation and to define pertinent input data to the simulator.

Consider a SAR system flying with constant velocity v at an altitude $R_o \cos \vartheta_o$ along the x direction (see Fig. 2). The SAR emits pulses at times t_n with linear frequency modulation:

$$\exp\left[j\omega(t-t_n) + j\frac{\alpha}{2}(t-t_n)^2\right] \cdot \operatorname{rect}\left[\frac{t_n - t}{\tau}\right] \tag{18}$$

wherein $\alpha\tau = 2\pi\Delta f$, Δf being the chirp bandwidth. Letting

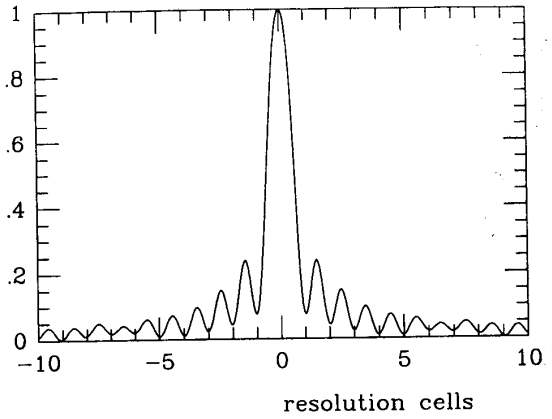

(a)

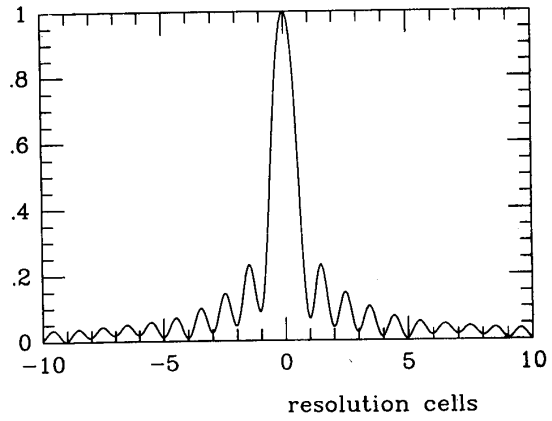

(b)

Fig. 7. Range cross-section (a) of the autocorrelation function of the image depicted in Fig. 5. For comparison, the cross-section of the image of a point scatterer (point spread function) is given (b).

$$t' = t - t_n - \frac{2R_o}{c} \tag{19}$$

the SAR raw signal exhibits the following form [9], after heterodyne,[1] for each polarization channel:

$$h\left(x' = vt_n,\ r' = \frac{ct'}{2}\right) = \iint dx\, dr\, \gamma(x,r) \cdot g(x'-x, r'-r;\ x, r) \tag{20}$$

wherein $\gamma(\cdot)$ is the equivalent backscattering coefficient of the scene, given by the appropriate value (8–10) depending on the polarization channel, and

$$g(x'-x, r'-r; x, r) = w^2\left(\frac{x'-x}{X}\right)\operatorname{rect}\left[\frac{r'-r}{c\tau/2}\right]\exp(j\phi) \tag{21}$$

$$\phi = -\frac{4\pi}{\lambda}\Delta R + \frac{\alpha}{2}\left(t' - \frac{2r}{c} - \frac{2\Delta R}{c}\right)^2 \tag{22}$$

[1]The variable x', which is discrete, is considered continuous as usual.

$$\Delta R = \sqrt{(x'-x)^2 + (R_o + r)^2 + s^2} - R_o - r. \quad (23)$$

In (21) $w(\cdot)$ is the (normalized) illumination footprint of the (real) antenna over the scene, wherein X is a convenient effective illumination size: For instance, we have $w(\cdot) = \mathrm{sinc}(\pi x/X)$ for a uniform aperture, $\pm X/2$ corresponding to the -3.9 dB points. Note explicitly that no approximation has been made, at this stage of the analysis, on the expression for the unit response $g(\cdot)$.

In order to simulate the raw signal (20), we first compute its Fourier transform (FT):

$$H(\xi,\eta) = \iint dx\, dr\, \gamma(x,r) G(\xi,\eta;\ x,r) \exp(-j\xi x - j\eta r) \quad (24)$$

wherein

$$G(\xi,\eta;\ x,r) = \iint dp\, dq\, g(p,q;\ x,r) \exp(-j\xi p - j\eta q) \quad (25)$$

is the FT of the unit response function $g(\cdot)$.

In [9] it is shown that the integral (25) exhibits a fast varying phase term and can be asymptotically evaluated via the stationary phase method.[2] Except for an inessential constant, we get

$$G(\xi,\eta;\ x,r) = \frac{d\left(\frac{\eta}{b^2}\right) w^2\left(-\frac{2\chi a^2 + \xi}{2a^2}\right)}{\sqrt{1 + \varepsilon\frac{\eta}{2b^2} - \frac{3}{2}\gamma^2\frac{\xi^2}{4a^4}}} \sqrt{1+\beta r}\exp(-j\psi) \quad (26)$$

$$\psi = \chi\xi + \frac{\eta^2}{4b^2} + \frac{\xi^2}{4a^2}\,\frac{1+\beta r}{1+\varepsilon\frac{\eta}{2b^2}}. \quad (27)$$

Equations (26) and (27) make use of normalized variables: ξ and η are normalized to $1/X$ and $2/c\tau$, respectively, so that their Fourier mates, x and r, are normalized to X and $c\tau/2$. The parameters:

$$a^2 = \frac{2\pi X^2}{\lambda R_o}, \qquad b^2 = \frac{\alpha\tau^2}{2} = \pi\frac{\Delta f}{f}\,\frac{c\tau}{\lambda} \quad (28)$$

are large quantities related to the (normalized) resolutions $\Delta x = \pi/a^2$, $\Delta r = \pi/b^2$. In particular, the large magnitude of a^2 allows the asymptotic evaluation discussed in [9].

The additional factors appearing in (27) are defined as follows:

$$\varepsilon = \frac{\Delta f}{f}; \qquad \beta = \frac{c\tau}{2R_o}; \qquad \gamma^2 = \left(\frac{X}{R_o}\right)^2 \quad (29)$$

$$\chi(x,r) = \frac{R_o}{X}\,[u_r + \beta r u_r + \gamma s u_s]. \quad (30)$$

Note the ϵ in a range–azimuth coupling factor due to the inclusion of the term ΔR in the last factor of (22); β is a focus-depth factor; and $2a^2\chi$ is the (normalized) Doppler centroid frequency [9] and depends on the u_r and u_s components of the (normalized to v) Earth surface velocity relative to the platform one. It is concluded that both range curvature and migration effects are properly included in the system transfer function $G(\cdot)$.

The function $d(\eta/b^2)$ is defined in [9] and can be easily computed in terms of Fresnel integrals. We have

$$\lim_{b^2\to\infty} d\left(\frac{\eta}{b^2}\right) = \mathrm{rect}\left[\frac{\eta}{2b^2}\right] \quad (31)$$

so that $d(\cdot)$ is close to a rectangular pulse in most practical cases.

If the direct dependence of $G(\cdot)$ upon the variable r can be neglected, then (24) becomes:

$$H(\xi,\eta) = G(\xi,\eta)\Gamma(\xi,\eta) \quad (32)$$

wherein $\Gamma(\xi,\eta)$ is the FT of an element of the ensemble of the stochastic process $\gamma(x,r)$, and

$$h(x',r') = \frac{1}{(2\pi)^2}\iint d\xi\, d\eta\, \Gamma(\xi,\eta) G(\xi,\eta) \cdot \exp(j\xi x' + j\eta r'). \quad (33)$$

Accordingly, efficient memory saving two-dimensional FFT codes can be used [9] for the evaluation of both $\Gamma(\cdot)$ and $h(\cdot)$. These codes are also amenable to a parallel implementation [28], if speed of computation is a major concern.

For a precision simulation it is desiderable to retain the direct r dependence in (24), meanwhile maintaining the convenient use of FFT codes [29]. This implies that the system focus depth is correctly included in the simulation. To this end, let us now put (26) in the following form:

$$G(\xi,\eta;\ x,r) = G_o(\xi,\eta)\sqrt{1+\beta r}\exp\left[-j\beta r\frac{\xi^2}{4a^2\left(1+\varepsilon\frac{\eta}{2b^2}\right)}\right] \approx G_o(\xi,\eta)\sqrt{1+\beta r}\exp\left[-j\beta\frac{\xi^2}{4a^2}r\right] \quad (34)$$

wherein $G_o(\xi,\eta)$ is the value of $G(\cdot)$ for $\beta = 0$. Use of (34) in (24) shows that

$$H(\xi,\eta) = \Gamma'(\xi',\eta')G_o(\xi,\eta) \quad (35)$$

wherein $\Gamma'(\cdot)$ is the FT of the modified reflection coefficient $\gamma(x,r)\sqrt{1+\beta r}$ in the output variables:

$$\begin{cases} \xi' = \xi \\ \eta' = \eta + \beta\frac{\xi^2}{4a^2} \end{cases} \quad (36)$$

which amounts to interpolating the desired values of $\Gamma'(\xi',\eta')$ from the available ones $\Gamma(\xi,\eta)$ [29]. Then, the SAR raw signal $h(x',r')$ is simply obtained by performing an (inverse) FFT.

V. Structure of the Digital Code

In the present section we briefly summarize how the theoretical results presented in previous sections have been implemented in the numerical code SARAS. The program has been written in Fortran-77 for a general purpose digital computer.

The scheme of the raw data simulator is depicted in Fig. 8. We note that the first level of the scheme is relative to the input

[2] The error in the asymptotic evaluation is of the order $\lambda R_o/2\pi X^2$, and, therefore, negligible in all practical cases. From this viewpoint, result (26) can be considered "exact". Note that application of asymptotic techniques in one dimension to SAR processing has been pioneered by Harger [27].

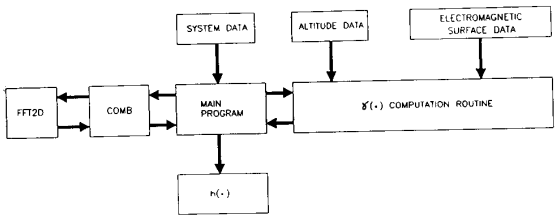

Fig. 8. SARAS architecture.

procedure; the second one logically shows computational routines; and the third one is related to the output procedure. The main program takes care of managing all different subroutines. First of all, the program requires the insertion of typical system parameters regarding the mission of the simulated; then, the electromagnetic and altitude characteristics of the scene under survey must be specified.

Input data are the following:

Mission data: spacecraft height, velocity, nominal look-angle; antenna parameters and polarization; carrier, sampling, and intermediate frequencies; pulse repetition rate and elapsing time, chirp bandwidth.

Scene characteristic data: altitude profile, electromagnetic parameters (ε_r, σ), statistical behavior, reirradiation diagram of the facets.

Once all the input data are inserted, scanning of the modeled surface is accomplished and the program generates the altitude grid map. Large-scale statistics is included as explained under Section III. Scanning is implemented for any equi-azimuth line, from near to far range, in order to use the ray-tracing recursive method to sort out the shadowed zones (see Section II).

A rather important point is the geometrical distortion: Input data are given on a uniform (x, y) grid, whereas output points are required again on uniform (x, r) grid. This implies that the facets' contributions should be properly mapped to the output grid.

Once the evaluation of $\gamma(\cdot)$ is accomplished, taking into account both deterministic and statistical input data, its two-dimensional FT $\Gamma(\cdot)$ is computed; this is done by means of the comb FFT routine [9]. Let us note that this two-dimensional FFT code described under Section IV is very convenient when a large amount of data must be handled, because it allows us to compute a very large two-dimensional FFT via a two-step procedure of smaller order FFT's, thus requiring a much smaller computer core memory. This algorithm allows an engineering compromise between the available core memory and time requirements.

Following the two-dimensional FFT of $\gamma(\cdot)$, multiplication by the transfer function $G(\cdot)$ is in order. After appropriate grid deformation (see Section IV), an inverse two-dimensional FFT is performed, again invoking the comb routine. Finally, some basic postprocessing, when desired, is accomplished in order to make results feasible for display.

Some information about computation time is now in order. Reference is made to the computer VAX 3100/30, running on VMS 5.1 operating system, used to develop and test our program. Simulation of 512 × 512 pixels raw signal as presented in the following, requires about 8′10″ CPU time if one facet per pixel has been used. Considering 2 × 2 facets per pixel the CPU time becomes 15′30″, while 3 × 3 facets correspond to 26′30″, and finally, simulation using 4 × 4 facets per pixel needs 41′20″ CPU time. Normal task conditions were considered.

Fig. 9. Speckled simulated raw signal of a cone over a flat background (HH polarization, $\varepsilon_r = 4, \sigma = 10^{-3}$ S/m).

VI. Examples

In this section we display some meaningful simulation examples generated by SARAS. In some cases, SARAS output data (i.e., the raw signal) are subsequently compressed [9] to obtain the corresponding displayed image. In all cases, the vertical direction is the along-track axis (azimuth), while the horizontal one is the across-track axis (range). The chosen number of facets per pixel is usually four.

The first example is aimed at displaying raw data and the overall performance of the simulator. The scene consists of a flat background with a superimposed cone. Electromagnetic parameters do not change over the area under survey. The reirradiation diagram is $\cos^2\delta$, which determines (see Section II) the roughness statistics of the facet. Statistical deformation of the grid map is accomplished assuming a height standard deviation $\sigma = 0, 10\lambda$. The real part of the raw data and the corresponding image are given under Figs. 9 and 10, respectively. We note the appearance of the well-known speckle phenomena as well as geometric distortion [30], due to the $(x, y, z) \rightarrow (x, r, s)$ coordinate transformation. This geometric distortion causes a slope-dependent shrinking or enlarging of the facets' dimension along the y-axis (see Fig. 11): Facets of constant size along the y-axis are no longer so along the r-axis. Geometric distortion moves higher facets in the direction of the illumination source.

The second example is aimed at displaying different models of roughness on a scene composed of different materials. A flat terrain is divided in 22 patches with homogeneous electromagnetic parameters. Four cases are considered:

Fig. 12(a): 4 × 4 facets per pixel, with both microscopic (rough facet) and macroscopic (rough profile, $\sigma = \lambda$) statistics;

Fig. 12(b): 4 × 4 facets per pixel, with only microscopic (rough facet, $\sigma = 0$) statistics;

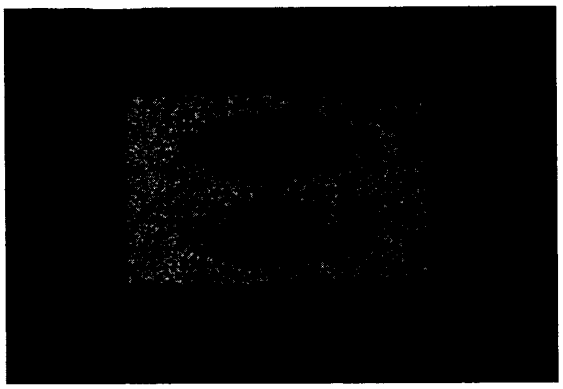

Fig. 10. SAR-simulated image of a cone over a flat background (HH polarization, $\varepsilon_r = 4, \sigma = 10^{-3}$ S/m).

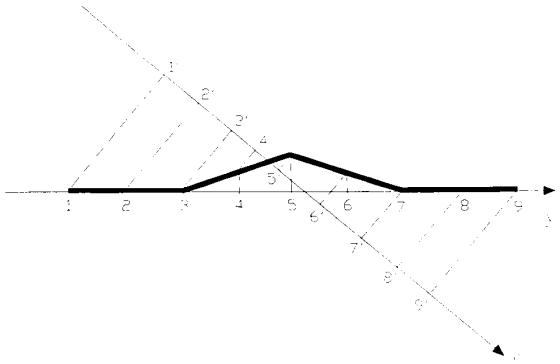

Fig. 11. Relevant to geometric distortion (uniform sampling along y-axis does not correspond to uniform sampling along r-axis).

Fig. 12(c): 4×16 facets per pixel, with only macroscopic (rough profile, $\sigma = \lambda$) statistics;

Fig. 12(d): 4×4 facets per pixel, with no statistics at all.

For all cases the corresponding grey level distribution relative to one of the patches is provided. Note that this distribution is Rayleigh for case A, B (as expected, Gaussian scene), but not for case C. Flexibility of the simulator is demonstrated: Further analysis in this area is advisable.

The third example is aimed at showing the simulator ability to handle layover and shadow phenomena. The scene (Fig. 13) consists of a parallelepiped, which casts a shadow over the flat background. Note that the shadow region is speckle free, as would be expected. Addition of the speckle directly over the image would not necessarily meet this requirement.

The fourth example is aimed at showing the polarimetric performance of the simulator (for this reason nonspeckled images are presented). The image of a cone over a flat background is presented, for different polarizations: HH (Fig. 14), VV (Fig. 15), and HV (Fig. 16). No marked differences are present between HH and VV cases, according to similar expressions for S_{HH} and S_{VV} appropriate to the case. On the contrary, quite different results are obtained for the HV case. This is to be expected, because we have maximum return when the wave propagation vector $\hat{\boldsymbol{k}}$ and the facet normal $\hat{\mathbf{n}}$ are parallel for the HH and VV polarization, and no return for the HV or VH polarization in this case. As a final check, the flat background correctly produces no return in the HV case. Note that an absolute grey tone level has not been used as common shade in Figs. 14–16.

As a last example, we display in Fig. 17 the image of a combination of a parallelepiped over a cylinder with a cone on the side, where altitude profile, shadow, layover, and speckle are all included.

VII. Final Discussion and Conclusions

In previous sections we presented the theory and the numerical implementation of the SAR signal simulator of a terrain scene. This simulator is based on a sound physical model which takes into account altitude profile together with shadows and layover, terrain electromagnetic properties together with frequency and polarization dependence, and small as well as large scale statistics. Use of the nonfactorized system transfer function in its analytical form allows easy conclusion of SAR aberrations such as range curvature and limited focus depth. Furthermore, the simulator output, which is the SAR raw signal, is efficiently generated via a two-stage FFT code, where the number of input points (facets) may be larger than the number of output points (pixels).

It has been verified that for a Gaussian scene the first-order statistics of the compressed (one look) image is Rayleigh and depends on the roughness parameters; the second-order statistics are determined by the SAR system bandwidth.

The code is modular: It can accept alternative models for the backscattered return, and it is amenable to parallel processing, if computer running time is a major concern. The code is also flexible, and can be modified for other type of scenes, such as the ocean or vegetated terrain (volume scattering).

Some last comments about the spatial bandwidths involved are in order. The raw signal has a bandwidth determined by the system transfer function $G(\xi, \eta)$, thus being inversely proportional to the resolution length. However, the bandwidth of $\Gamma(\xi, \eta)$, the FT of the reflecitivity pattern $\gamma(x, r)$, is much larger. As a matter of fact, $\gamma(x, r)$ is a stochastic process, and the bandwidth of its power spectrum is determined (and inversely proportional) to its correlation length L. This, in turn, is usually much smaller than the resolution, which accounts for the larger bandwidth of $\Gamma(\cdot)$ compared to $G(\cdot)$.

When we make the FT of one element of the ensemble of $\gamma(\cdot)$, only its output within the bandwidth of $G(\cdot)$ is required; the number of output points should be consistent with the Nyquist rate to recover the FT $h(\cdot)$ of the bandlimited function $\Gamma(\cdot)G(\cdot)$. However, the correct evaluation of the FT $\Gamma(\cdot)$ requires in principle a much larger bandwidth. This is another way of stating the necessity of facet segmentation larger than one pixel (see Section III). In our code we can increase the number of facets per resolution cell (see Section IV), alleviating computer memory requirement. And the finer grain change of $\gamma(\cdot)$ is somehow taken into account by the (small-scale) microscopic characterization of a single facet's return (see Section II). A large increase in facet number

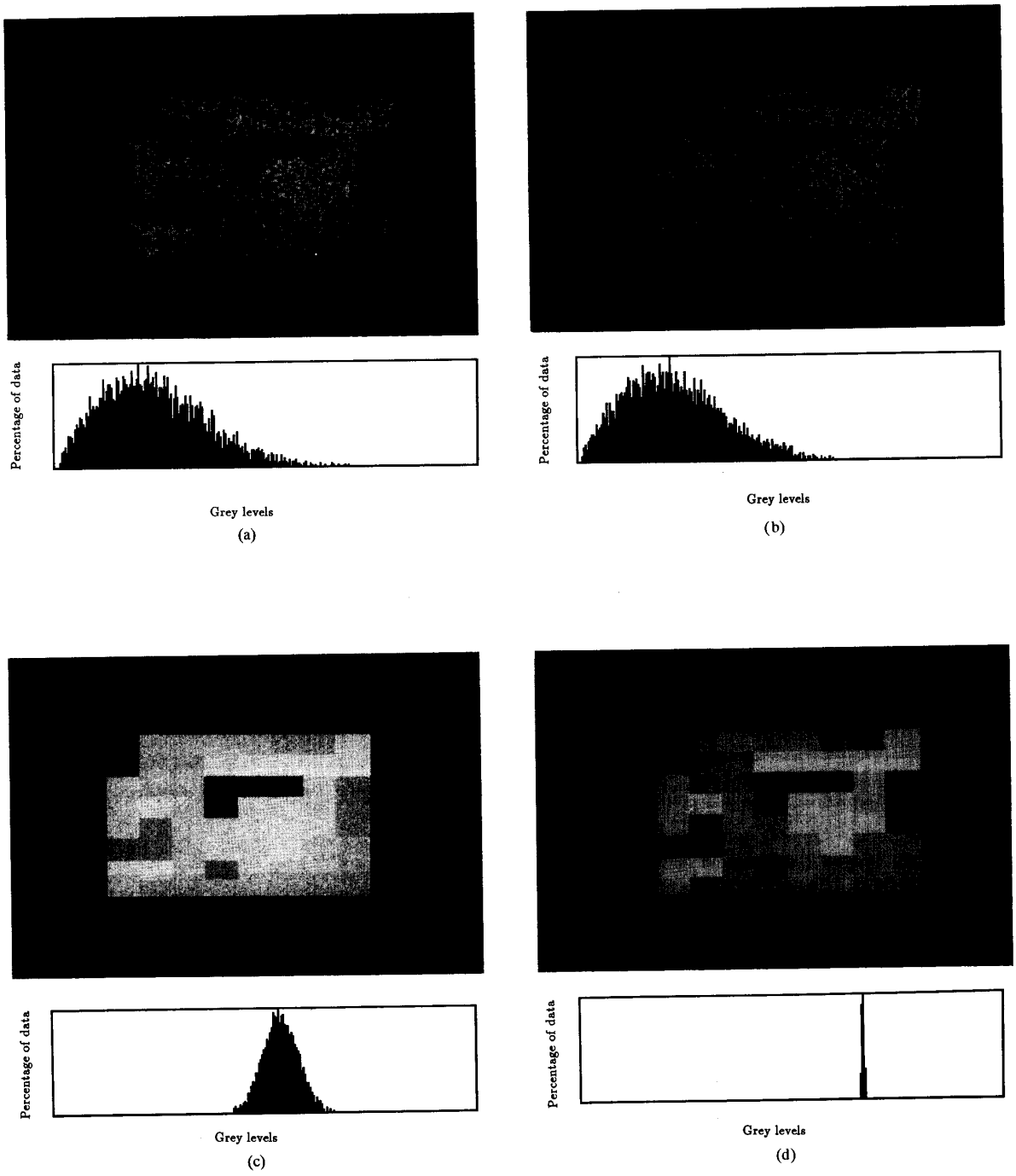

Fig. 12. Image of a flat terrain composed of 22 patches with different electromagnetic parameters: relative permittivity ranging from 1 to 40 and conductivity ranging from 10^{-4} S/m to 1 S/m. (a) 4×4 facets per pixel, rough facet, rough profile ($\sigma = \lambda$). (b) 4×4 facets per pixel, rough facet. (c) 4×16 facets per pixel, with only macroscopic statistics ($\sigma = \lambda$). (d) 4×4 facets per pixel, with no statistics at all. For all cases the corresponding grey-level distribution relative to the lower left-hand corner homogeneous patch is provided.

obviously increases the computational time. Should this be a major concern, parallel processing techniques can easily be implemented.

This discussion points out the relevance of the statistical nature of backscattered return and its implication in the formation of SAR raw signals. Thus, one wonders if alternative simulation techniques may be foreseen, and may be more efficient than the classical ones exploited in this paper. We make some preliminary comments on this question as recommendations for future research.

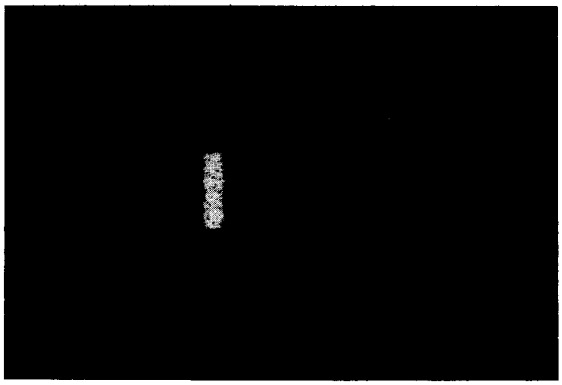

Fig. 13. SAR-simulated image of a parallelepiped over a flat background (HH polarization, $\varepsilon_r = 4, \sigma = 10^{-3}$ S/m).

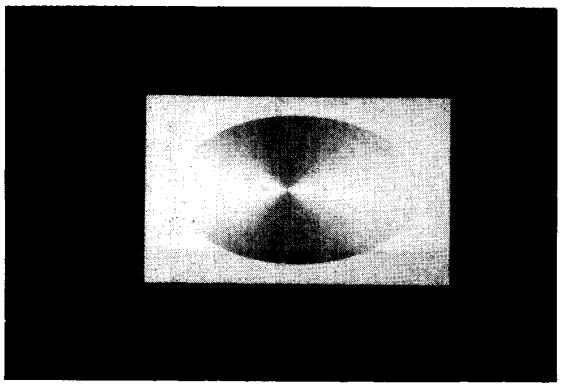

Fig. 14. Non-speckled simulated image of a cone over a flat background (HH polarization, $\varepsilon_r = 4, \sigma = 10^{-3}$ S/m).

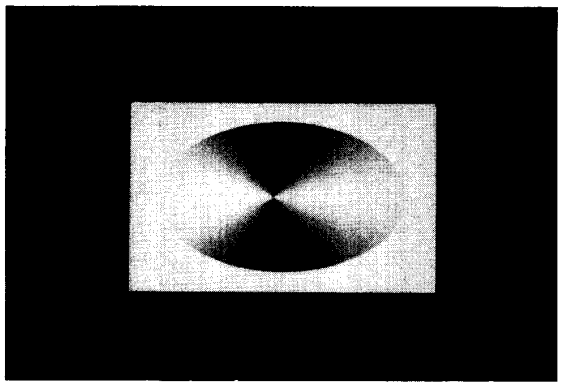

Fig. 15. Non-speckled simulated image of a cone over a flat background (VV polarization, $\varepsilon_r = 4, \sigma = 10^{-3}$ S/m).

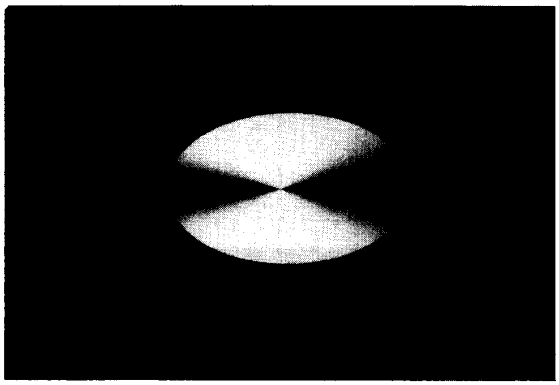

Fig. 16. Non-speckled simulated image of a cone over a flat background (HV polarization, S/m).

The problem at hand can be stated in its simplified one-dimensional form as follows: to compute the integral

$$h(x') = \int \gamma(x) \exp\left[ja^2(x - x')^2\right] \operatorname{rect}[x - x']\, dx \quad (37)$$

wherein a^2 is a large number and $\gamma(x)$ exhibits a random phase term.

Major contributions to the integral $h(x')$ arise from the stationary phase points:

$$x_s = x' + \frac{\dot{\Psi}}{2a^2} \quad (38)$$

wherein a dot implies derivative operation with respect to x. For each output point x', (38) states the width around the integration point $x = x'$ within which major contributions to the integral (37) may arise. This width depends upon the statistical properties of $\dot{\Psi}$ as well as on the normalized system resolution π/a^2.

If we take Ψ to be Gaussian distributed with zero mean and variance σ^2, it is known that $\dot{\Psi}$ is also Gaussian distributed with zero mean and variance $2\sigma^2/L^2$, L being the correlation length of the stochastic process Ψ. Taking $\pm\sqrt{2}\,\sigma/L$ as $\dot{\Psi}$ spread, it is easy to show that integration of (37) around x' can be limited to a width $\pm(\phi/\pi)(\Delta x/L)$, wherein Δx is the resolution length. This suggests the use of a traveling convolution of limited extent for the efficient computation of (37), as well as a way to introduce the correlation length of $\gamma(\cdot)$ in the simulation.

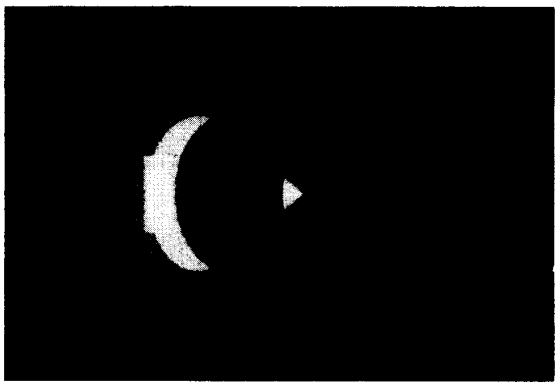

Fig. 17. SAR-simulated image of a combination of a parallelepiped over a cylinder with a cone on the side.

APPENDIX
COMPUTATION OF THE POLARIZATION MATRIX

We explicitly compute hereafter the entries of the polarization matrix $\underline{\underline{S}}$ given by (7). It is useful to use the natural orthonormal system (x, r, s) of Fig. 2. We have

$$\boldsymbol{n} = (a, b, c)$$

with

$$a = \frac{\partial z(x,y)}{\partial x}, \qquad b = \frac{\partial z(x,y)}{\partial r}, \qquad c = \frac{\partial z(x,y)}{\partial s} \tag{A.1}$$

so that (3) can be evaluated as shown below.
In (A.2) and (A.3) we have

$$\Delta\vartheta = \vartheta - \vartheta_o \tag{A.4}$$

ϑ_o being the nominal look-angle referred to the center of the footprint, while ϑ is the effective look-angle (see Fig. 2) referred to the center of the facet considered. Note that the incident direction $\hat{\boldsymbol{k}}$ is not parallel to $\hat{\boldsymbol{r}}$ (except for the center of the scene), thus requiring the consideration of the effective look angle θ instead of θ_o.

Strictly speaking, $\hat{\boldsymbol{k}}$ is not orthogonal to $\hat{\boldsymbol{x}}$ (except for the center of the scene), which implies that the backscattering coefficient (see (20)) is a function of the platform coordinate x'. This makes the SAR raw signal computation more complicated, suggesting that we neglect the small variation of the incidence angle δ—see subsequent (A.8)—and that we assume $\hat{\mathbf{k}}$ orthogonal to $\hat{\mathbf{x}}$.

At this point we treat the H and V polarization cases separately, computing the appropriate components of $\boldsymbol{F}(a, b, c)$, hence

$$\begin{aligned}
\mathbf{F}_V(a,b,c) = \{&[2a(R_p + R_q)(c\sin\Delta\vartheta - b\cos\Delta\vartheta) \\
&\cdot (c\cos\Delta\vartheta + b\sin\Delta\vartheta)]\hat{\mathbf{x}} \\
&+ [(c\sin\Delta\vartheta - b\cos\Delta\vartheta)\sin\Delta\vartheta\Big((c\cos\Delta\vartheta + b\sin\Delta\vartheta)^2 \\
&\cdot (1 - R_q) - 2a^2R_p\Big) \\
&+ (1 + R_q)(c\cos\Delta\vartheta + b\sin\Delta\vartheta)(a^2\cos\Delta\vartheta + (c\cos\Delta\vartheta \\
&+ b\sin\Delta\vartheta)c)]\hat{\boldsymbol{r}} \\
&+ [(c\sin\Delta\vartheta - b\cos\Delta\vartheta)\cos\Delta\vartheta\Big((c\cos\Delta\vartheta + b\sin\Delta\vartheta)^2 \\
&\cdot (1 - R_q) - 2a^2R_p\Big) \\
&- (1 + R_q)(c\cos\Delta\vartheta + b\sin\Delta\vartheta)(a^2\sin\Delta\vartheta + (c\cos\Delta\vartheta \\
&+ b\sin\Delta\vartheta)b)]\hat{\boldsymbol{s}}\} \\
&\cdot\Big[a^2 + (b\sin\Delta\vartheta + c\cos\Delta\vartheta)^2\Big]^{-1}
\end{aligned} \tag{A.5}$$

$$\begin{aligned}
\mathbf{F}_H(a,b,c) = \{&\Big[2(b\cos\Delta\vartheta - c\sin\Delta\vartheta) \\
&\cdot \Big(-R_qa^2 + (b\sin\Delta\vartheta + c\cos\Delta\vartheta)^2R_p\Big)\Big]\hat{\boldsymbol{x}} \\
&+ [(c\cos\Delta\vartheta + b\sin\Delta\vartheta)((b\cos\Delta\vartheta - c\sin\Delta\vartheta) \\
&\cdot (-a\sin\Delta\vartheta)2R_p \\
&+ ac(1 + R_q) + a\sin\Delta\vartheta(b\cos\Delta\vartheta - c\sin\Delta\vartheta) \\
&\cdot (1 - R_q)) + a^3\cos\Delta\vartheta(1 + R_q)]\hat{\boldsymbol{r}} \\
&+ [(c\cos\Delta\vartheta + b\sin\Delta\vartheta)((b\cos\Delta\vartheta - c\sin\Delta\vartheta) \\
&\cdot (-a\cos\Delta\vartheta)2R_p \\
&- ab(1 + R_q) + a\cos\Delta\vartheta(b\cos\Delta\vartheta - c\sin\Delta\vartheta)(1 - R_q)) \\
&- a^3\sin\Delta\vartheta(1 + R_q)]\hat{\mathbf{s}}\} \\
&\cdot\Big[a^2 + (b\sin\Delta\vartheta + c\cos\Delta\vartheta)^2\Big]^{-1}
\end{aligned} \tag{A.6}$$

wherein

$$\begin{aligned}
R_p &= \frac{\cos\delta - \sqrt{\varepsilon_r - \sin^2\delta}}{\cos\delta + \sqrt{\varepsilon_r - \sin^2\delta}}; \\
R_q &= \frac{\sqrt{\varepsilon_r - \sin^2\delta} - \varepsilon_r - \cos\delta}{\sqrt{\varepsilon_r - \sin^2\delta} + \varepsilon_r - \cos\delta}
\end{aligned} \tag{A.7}$$

are Fresnel reflection coefficients for the two polarizations, and

$$\cos\delta = \hat{\mathbf{n}}\cdot\hat{\mathbf{k}} \tag{A.8}$$

The entries of the matrix $\boldsymbol{S}$ (7) are now obtained by dot multiplication by $\Big(\underline{\underline{I}} - \hat{\mathbf{k}}\hat{\mathbf{k}}\Big)$. In the (x, r, s) coordinate system we get

$$\begin{aligned}
S_{Hx} &= \boldsymbol{F}_H\cdot\hat{\boldsymbol{x}} \\
S_{Hr} &= (\boldsymbol{F}_H\cdot\hat{\boldsymbol{r}}\sin\Delta\vartheta + \boldsymbol{F}_H\cdot\hat{\boldsymbol{s}}\cos\Delta\vartheta)\sin\Delta\vartheta \\
S_{Hs} &= (\boldsymbol{F}_H\cdot\hat{\boldsymbol{r}}\sin\Delta\vartheta + \boldsymbol{F}_H\cdot\hat{\boldsymbol{s}}\cos\Delta\vartheta)\cos\Delta\vartheta
\end{aligned} \tag{A.9}$$

and

$$\begin{aligned}
S_{Vx} &= \boldsymbol{F}_V\cdot\hat{\boldsymbol{x}} \\
S_{Vr} &= (\boldsymbol{F}_V\cdot\hat{\boldsymbol{r}}\sin\Delta\vartheta + \boldsymbol{F}_V\cdot\hat{\boldsymbol{s}}\cos\Delta\vartheta)\sin\Delta\vartheta \\
S_{Vs} &= (\boldsymbol{F}_V\cdot\hat{\boldsymbol{r}}\sin\Delta\vartheta + \boldsymbol{F}_V\cdot\hat{\boldsymbol{s}}\cos\Delta\vartheta)\cos\Delta\vartheta.
\end{aligned} \tag{A.10}$$

We recall now that $\hat{\boldsymbol{k}}$ is not parallel to $\hat{\boldsymbol{r}}$, but approximately orthogonal to $\hat{\boldsymbol{x}}$. The H-polarized part of received fields is along the x-axis, so that

$$\begin{aligned}
S_{HH} &= S_{Hx} \\
S_{VH} &= S_{Vx}.
\end{aligned} \tag{A.11}$$

$$\hat{\boldsymbol{p}} = \frac{a\hat{\boldsymbol{x}} + (c\sin\Delta\vartheta\cos\Delta\vartheta + b\sin^2\Delta\vartheta)\hat{\boldsymbol{r}} + (c\cos^2\Delta\vartheta + b\sin\Delta\vartheta\cos\Delta\vartheta)\hat{\boldsymbol{s}}}{\sqrt{a^2 + (b\sin\Delta\vartheta + c\cos\Delta\vartheta)^2}} \tag{A.2}$$

$$\hat{\boldsymbol{q}} = \frac{(c\cos\Delta\vartheta + b\sin\Delta\vartheta)\hat{\boldsymbol{x}} - (a\sin\Delta\vartheta)\hat{\boldsymbol{r}} - (a\cos\Delta\vartheta)\hat{\boldsymbol{s}}}{\sqrt{a^2 + (b\sin\Delta\vartheta + c\cos\Delta\vartheta)^2}}. \tag{A.3}$$

This is at variance with V-polarized received fields, which possess both r and s components, so that

$$S_{HV}\hat{\boldsymbol{k}}\times\hat{\boldsymbol{x}} = S_{Hr}\hat{\boldsymbol{r}} + S_{Hs}\hat{\boldsymbol{s}};$$
$$S_{HV} = \frac{S_{Hr}}{\sin\Delta\vartheta} = \frac{S_{Hs}}{\cos\Delta\vartheta}$$
$$S_{VV}\hat{\boldsymbol{k}}\times\hat{\boldsymbol{x}} = S_{Vr}\hat{\boldsymbol{r}} + S_{Vs}\hat{\boldsymbol{s}};$$
$$S_{VV} = \frac{S_{Vr}}{\sin\Delta\vartheta} = \frac{S_{Vs}}{\cos\Delta\vartheta}. \tag{A.12}$$

Inserting (A.5–6, 9–10) in (A.11–12) we obtain

$$S_{HH} = \frac{2(c\sin\Delta\vartheta - b\cos\Delta\vartheta)}{a^2 + (b\sin\Delta\vartheta + c\cos\Delta\vartheta)^2} \cdot \left[a^2R_q - (b\sin\Delta\vartheta + c\cos\Delta\vartheta)^2R_p\right] \tag{A.13}$$

$$S_{VH} = S_{HV} = \frac{2a(c\sin\Delta\vartheta - b\cos\Delta\vartheta)(b\sin\Delta\vartheta + c\cos\Delta\vartheta)}{a^2 + (b\sin\Delta\vartheta + c\cos\Delta\vartheta)^2} \cdot (R_p + R_q) \tag{A.14}$$

$$S_{VV} = \frac{2(c\sin\Delta\vartheta - b\cos\Delta\vartheta)}{a^2 + (b\sin\Delta\vartheta + c\cos\Delta\vartheta)^2} \cdot \left[(b\sin\Delta\vartheta + c\cos\Delta\vartheta)^2R_q - a^2R_p\right]. \tag{A.15}$$

As proof of validity of the obtained results, we have $S_{HV} = S_{VH}$ as expected.

REFERENCES

[1] J. C. Holtzman, V. S. Frost, J. L. Abbott, and V. H. Kaupp, "Radar image simulation," *IEEE Trans. Geosci. Remote Sensing, GE-16*, pp. 296–303, 1978.

[2] J. M. Blackledge, "Theory of imaging with airborne synthetic aperture radar," *Optik, 78*, pp. 1–11, 1987.

[3] P. Hartl, M. J. Nahvi, S. Rieger, W. Wiesbeck, M. S. Sciver, D. G. Corr, and A. J. Sieber, "Simulation of synthetic aperture radar data products," in *Proc. SAR Applications Workshop*, Frascati, Italy, Sept. 16–18, 1986.

[4] T. K. Pike, "SARSIM: A synthetic aperture radar system simulation model," *DFVLR-Mitteilung* 85–11, 1985.

[5] R. J. Brown and C. A. Hutton, "Simulation of satellite SAR imagery," in *Proc. IGARSS '91*, Espoo, Finland, June 3–6, 1991.

[6] F. T. Ulaby and M. C. Dobson, *Handbook of Radar Scattering Statistics for Terrain*. Norwood, MA, Artech House, 1989.

[7] K. Ouchi, S. Tajbakhsh, and R. E. Burge, "Dependence of speckle statistics on backscatter cross-section fluctuations in synthetic aperture radar images of rough surfaces," *IEEE Trans. Geosci. Remote Sensing, GE-25*, pp. 623–628, 1987.

[8] R. K. Raney and G. J. Wessels, "Spatial considerations in SAR speckle simulation," *IEEE Trans. Geosci. Remote Sensing, GE-26*, 1988.

[9] G. Franceschetti and G. Schirinzi, "A SAR processor based on two-dimensional FFT codes," *IEEE Trans. Aerosp. Electron. Syst., AES-26*, pp. 356–366, 1990.

[10] L. Tsang, J. A. Kong and R. T. Shin, *Theory of Microwave Remote Sensing*. New York: Wiley-Interscience, 1985.

[11] P. Beckmann and A. Spizzichino, *The Scattering of Electromagnetic Waves from Rough Surface*. Norwood, MA: Artech House, 1987.

[12] R. J. Papa and J. F. Lennon, "The dependence of rough surface scattering on surface height stochastics and correlation function," *IEEE Trans. Antennas Propagat., AP-35*, pp. 239–242, 1987.

[13] F. T. Ulaby, R. K. Moore, and A. K. Fung, *Microwave Remote Sensing*, vol. II, Reading, MA: Addison-Wesley, 1982.

[14] F. T. Ulaby, R. K. Moore, and A. K. Fung, *Microwave Remote Sensing*, vol. III. Norwood, MA: Artech House, 1986.

[15] T. F. Bush and F. T. Ulaby, "Fading characteristics of panchromatic radar backscatter from selected agricultural targets," *IEEE Trans. Geosci. Electr., GE-13*, pp. 149–157, 1975.

[16] M. I. Skolnik, *Introduction to Radar Systems*. New York: McGraw Hill, 1980.

[17] K. Hasselmann, R. K. Raney, W. J. Plant, W. Alpers, R. A. Shuchman, D. R. Lyzenga, C. L. Rufenach, and M. J. Tucker, "Theory of synthetic aperture radar ocean imaging: a MARSEN view," *J. Geophys. Res., 90*, pp. 4659–4686, 1985.

[18] R. L. Mitchell, *Radar Signal Simulation*. New York: Artech House, 1976.

[19] A. Papoulis, *Probability, random variables, and stochastic process*. New York: McGraw Hill, 1984.

[20] B. C. Barber, "Some properties of SAR speckle," in *Satellite Microwave Remote Sensing*, T. D. Allow, Ed. Chichester, West Sussex, England: Ellis Horwood, 1983, pp. 129–145.

[21] R. K. Raney, "Theory and measure of certain image norms in SAR," *IEEE Trans. Geosci. Remote Sensing, GE-23*, pp. 343–348, 1985.

[22] J. W. Goodman, "Some fundamental properties of speckle," *J. Opt. Soc. Am., 66*, pp. 1145–1150, 1976.

[23] J. W Goodman, *Statistical Optics*. New York: Wiley Interscience, 1985.

[24] L. J. Porcello, N. G. Massey, R. B. Innes, and J. M. Marks, "Speckle reduction in synthetic-aperture radars," *J. Opt. Soc. Am., 66*, pp. 1305–1311, 1976.

[25] A. Lopes, R. Touzi, and E. Nezry, "Adaptive speckle filters and scene heterogeneity," *IEEE Trans. Geosci. Remote Sensing, GE-28*, pp. 992–1000, 1990.

[26] K. Tomiyasu, "Computer simulation of speckle in a synthetic aperture radar image pixel," *IEEE Trans. Geosci. Remote Sensing, GE-21*, pp. 357–363, 1983.

[27] R. O. Harger, *Synthetic Aperture Radar Systems: Theory and Design*. New York: Academic Press, 1970.

[28] G. Franceschetti, A. Mazzeo, N. Mazzocca, V. Pascazio, and G. Schirinzi, "An efficient SAR parallel processor," *IEEE Trans. Aerosp. Electron. Syst., AES-27*, pp. 343–353, 1991.

[29] G. Franceschetti, R. Lanari, V. Pascazio, and G. Schirinzi, "WASAR: a wide angle SAR processor," in print on *Proc. IEE* part F.

[30] C. Elachi, *Introduction to the Physics and Techniques of Remote Sensing*. New York: Wiley-Interscience, 1987.

Giorgio Franceschetti (S'60–M'62–SM'73–F'88) was born and educated in Italy.

Winner of a national competition in 1968, he was appointed full Professor of Electromagnetic Wave Theory at University of Naples, Italy. In addition, he has been Visiting Professor at the University of Illinois (1976 and 1977) and at UCLA (1980 and 1982), USA; Fulbright Scholar (1973) and Research Associate (1981 and 1983) at Caltech, USA; Visiting Professor at National Somali University (1984), Somalia. He has published widely in the field of applied electromagnetics (reflector antennas, transient phenomena, shielding, nonlinear propagation and scattering) and, more recently, in the field of SAR data processing. He has lectured in several summer schools (University of Southern California, USA; Queen Mary College, London; Eindhoven Institute of Technology, The Netherlands). He has been invited to lecture at Ericsson, at the Chalmes Institute of Technology (Gotemberg, Sweden), at the Chinese Academy of Sciences and at the Chinese Academy of Space Technology. He is a scientific consultant to several companies in the US and Italy.

Dr. Franceschetti is a Fellow of IEEE and Director of IRECE, a research Institute of CNR, the Italian National Council of Research.

Maurizio Migliaccio (M'91) was born and educated in Italy. He graduated in electronic engineering at the University of Napoli (Italy) in 1987.

As a graduate student he joined the Department of Electronic Engineering of the same University. In 1989 he won a grant at IRECE (Napoli), an Institute of Italian National Council of Research, regarding SAR simulation. Since 1990 he has been a researcher of the Naval Universitary Institute of Napoli. His main scientific activities are devoted to Synthetic Aperture Radar simulation.

Daniele Riccio (M'91) was born in Napoli (Italy) in 1962. He graduated in electronic engineering at the University of Napoli in 1989.

In February, 1989 he joined the Department of Electronic Engineering of the same University. In October, 1989 he won a grant at IRECE (Napoli), an Institute of Italian National Council of Research. His main scientific interests and research activities are in the field of Synthetic Aperture Radar simulation.

Gilda Schirinzi (M'91) was born in Italy and graduated in electronic engineering at the University of Naples, Italy.

From 1983 to 1985 she worked at the Department of Electronic Engineering of the University of Naples on the application of sampling series to the electromagnetic field representation and near field-far field transformation. From 1985 to 1986 she was at the European Space Agency, ESTEC, the Netherlands. In 1988 she joined IRECE, a Research Institute of the Italian National Council of Research. Her main scientific interests are synthetic aperture radar simulation and processing.